

See discussions, stats, and author profiles for this publication at: <https://www.researchgate.net/publication/235968435>

Investigation of a Conjugated Polyelectrolyte Interlayer for Inverted Polymer:Fullerene Solar Cells

ARTICLE in ADVANCED ENERGY MATERIALS · JUNE 2013

Impact Factor: 16.15 · DOI: 10.1002/aenm.201200967

CITATIONS

37

READS

73

13 AUTHORS, INCLUDING:



Ruidong Xia

Nanjing University of Posts and Telecomm...

59 PUBLICATIONS 1,403 CITATIONS

SEE PROFILE



Dong-Seok Leem

Samsung Advanced Institute of Technology

69 PUBLICATIONS 1,429 CITATIONS

SEE PROFILE



Thomas Kirchartz

Forschungszentrum Jülich

92 PUBLICATIONS 1,996 CITATIONS

SEE PROFILE



Donal D. C. Bradley

University of Oxford

660 PUBLICATIONS 46,029 CITATIONS

SEE PROFILE

Investigation of a Conjugated Polyelectrolyte Interlayer for Inverted Polymer:Fullerene Solar Cells

Ruidong Xia,* Dong-Seok Leem, Thomas Kirchartz, Steve Spencer, Craig Murphy, Zhicai He, Hongbin Wu, Shijian Su, Yong Cao, Ji Seon Kim, John C. deMello, Donal D.C. Bradley, and Jenny Nelson

Organic solar cells (OSCs) have emerged as a promising technology for low-cost renewable energy generation due to their potential for high throughput manufacturing on lightweight flexible substrates by solution fabrication methods. Over the last decade, the most widely investigated OSC device configuration has been a bulk heterojunction (BHJ) active layer atop a poly(3,4-ethylenedioxythiophene):poly(styrenesulfonate) (PEDOT:PSS)/indium tin oxide (ITO) anode coated glass substrate, capped by a low-work-function aluminum cathode.^[1–6] In recent years, considerable efforts have been made to develop OSCs that can achieve a high power conversion efficiency (PCE) while maintaining good ambient stability.^[7–10] One of the most important developments related to stability has been the introduction of an inverted device geometry that avoids the use of reactive metals such as Ba and Ca at the electron collecting electrode. In the inverted geometry, metal oxides such as TiO_x and ZnO coated on top of ITO are generally used instead, with MoO_3/Ag or PEDOT:PSS/Au as the hole collecting electrode.^[11–17] It has also been reported that incorporating a conjugated poly-

electrolyte (CP) interlayer between the cathodic electrode and the organic active layer in a solar cell can improve device performance by changing the electronic and orbital interactions at the interfaces.^[18–22] Moreover, CPs support solution processed fabrication of multilayer OSCs due to their solubility in polar solvents.

Whilst CP materials have been widely reported to increase OSC efficiency, much less attention has been paid to understanding the mechanism of their beneficial influence. We report, herein, a detailed study of the improvements in device performance achieved with the use of a solution processed CP cathode interlayer. Changes in the ITO work function, the contact properties and the transmittance of the electrode are investigated. Using numerical simulations of the current voltage curves at different PFN layer thicknesses, we show that the change in workfunction measured with ultraviolet photoelectron spectroscopy (UPS) is consistent with the observed large shifts in open-circuit voltage V_{oc} . For uncoated ITO and for low CP thicknesses ($d < 3.5$ nm), the difference between the workfunction of the cathode and the electron affinity E_a of the fullerene is too large leading to a relatively high concentration of holes at the cathode that recombine with electrons in the cathode and reduce V_{oc} below the built in voltage, V_{bi} . Only with thicker CP interlayers are the benefits fully realised.

The bulk heterojunction active layer used in this study was a blend of Poly[N-9"-hepta-decanyl-2,7-carbazole-alt-5,5-(4',7'-di-2-thienyl-2',1',3'-benzothiadiazole)] (PCDTBT) as electron-donating conjugated polymer and [6,6]-phenyl- C_{70} -butyric acid methyl ester (PC_{70}BM) as electron-accepting fullerene (see Supporting Information Scheme S1a and S1b for the molecular structure and Figure S1a for absorption coefficient). PCDTBT is a widely studied conjugated polymer that has been used for both thin film transistors and OSCs.^[23–26] The CP interlayer used was the previously reported poly[(9,9-bis(3'-(N,N-dimethylamino)propyl)-2,7-fluorene)-alt-2,7-(9,9-dioctylfluorene)] (PFN) (see Supporting Information Scheme S1c for the molecular structure and Figure S1b for absorption coefficient and photoluminescence spectra).^[18] Our inverted OSC device structures comprised glass/ITO/PFN/PCDTBT: PC_{70}BM (1:2 by weight)/ MoO_3/Ag and were compared to standard (non-inverted) glass/ITO/PEDOT:PSS/PCDTBT: PC_{70}BM (1:2)/Ca/Al reference devices.

An interlayer thickness of less than 5 nm may not fully cover the ITO (average surface roughness ≈ 4 nm), leading to significant shorting issues, with low shunt resistances, high dark

Dr. R. Xia,^[†] Dr. T. Kirchartz, Dr. J. S. Kim,
Prof. D. D. C. Bradley, Prof. J. Nelson
Department of Physics and Centre for Plastic Electronics
Blackett Laboratory, Imperial College London
London SW7 2BZ, United Kingdom
E-mail: ruidong.xia@gmail.com;
jenny.nelson@imperial.ac.uk; D.Bradley@imperial.ac.uk
Dr. D.-S. Leem,^[‡] Prof. J. C. deMello
Department of Chemistry and Centre for Plastic Electronics
Imperial College London
Prince Consort Road, London, SW7 2BW, United Kingdom
S. Spencer, Dr. C. Murphy
National Physical Laboratory
Teddington, Middlesex TW11 0LW, United Kingdom
Mr. Z. He, Prof. H. Wu, Prof. S. Su, Prof. Y. Cao
Institute of Polymer Optoelectronic Materials and Devices
State Key Laboratory of Luminescent Materials and Devices
South China University of Technology, Guangzhou 510640, China
[†] Present Address: Key Laboratory for Organic Electronics & Information Displays (KLOEID), Institute of Advanced Materials (IAM), Nanjing University of Posts and Telecommunications, 9 Wenyuan Road, Nanjing 210046, China
[‡] Current address: Display Devices Laboratory, Samsung Advanced Institute of Technology (SAIT), Republic of Korea



DOI: 10.1002/aenm.201200967

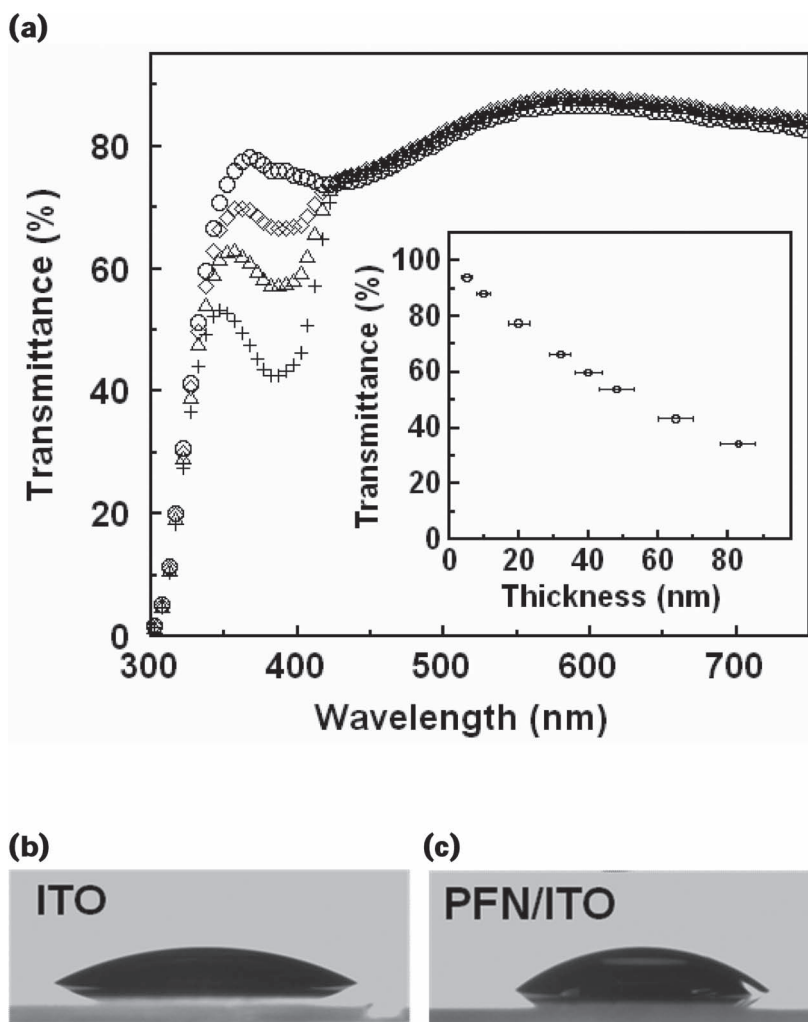


Figure 1. (a) The transmittance of ITO coated glass with 0 (open circles), 10 (open diamonds), 20 (open triangles) and 40 nm (crosses) thick PFN films deposited on top. Inset is the deduced film thickness dependence (after accounting for the ITO coated glass absorption) of the transmittance of PFN at its $\lambda = 400$ nm absorption peak. (b) Water contact angles measured on a bare ITO surface and (c) on ITO coated with a 10 nm thick PFN film.

currents at low forward and reverse bias and poor overall device efficiency. Introduction of the CP interlayer should not, however, materially reduce the electrode transparency and because, unlike more conventional PEDOT:PSS or TiO_2 layers, PFN has a strong optical absorption band at ≈ 400 nm (Figure S1b) this implies use of a thin layer. Selection of a suitable thickness for the PFN interlayer needs, therefore, to balance surface coverage and transparency requirements. **Figure 1a** shows the transmittance spectra of an ITO/glass substrate before and after coating with 10, 20 and 40 nm thick PFN layers. The PFN/ITO/glass stack retains high transmittance, greater than 80%, between ~ 475 and 800 nm for each of these thicknesses, but it drops to $\sim 42\%$ in the region of PFN absorption for the 40 nm coating. The inset to **Figure 1a** shows the thickness-dependence of the $\lambda = 400$ nm PFN transmittance (after correction for the ITO coated glass). It is clear that the PFN layer needs to be as thin as possible consistent with good surface coverage. We also studied the sheet resistance, R , of the coated ITO as a function

of PFN thickness using a four-point probe measurement system. We found no detectable change in ITO sheet resistance for ≤ 10 nm PFN. However, R does increase for higher PFN thicknesses. Thus, combining these results, in order to yield suitable OSC device performance we would seem to be restricted to using a PFN layer thickness in the range 5–10 nm.

Next, water contact angle (θ) measurements were performed on PFN coated ITO surfaces. The contact angle increased from 42.4° before coating to 51° with a 10 nm PFN coating (**Figure 1b** and **Figure 1c**). The increase in the contact angle indicates a more hydrophobic surface, which enhances wetting by organic solvents and is, therefore, beneficial for subsequent polymer active layer deposition.^[12]

One of the most important factors affecting device performance is charge carrier extraction from the polymer:fullerene photogeneration layer. In an inverted OSC, electrons are extracted at the ITO cathode and consequently recombination of holes at the cathode has to be suppressed to achieve good device performance. The recombination current of holes at the cathode is normally assumed to be proportional to the concentration of holes at the cathode. We can express the equilibrium concentration p_0 as

$$p_0 = N_V \exp\left(\frac{\phi_{\text{cath}} - E_{\text{gi}}}{kT}\right) \quad (1)$$

with N_V the effective density of states for holes, $\phi_{\text{cath}} = WF_{\text{cath}} - E_{\text{a,PCBM}}$, $E_{\text{gi}} = IP_{\text{PCDTBT}} - E_{\text{a,PCBM}}$ is the interfacial band gap, IP the ionization potential, kT the thermal energy, and WF_{cath} the cathode workfunction (see **Figure 2a**). From Equation (1), we see that a

large contact barrier ϕ_{cath} leads to a large p_0 and consequently a large hole concentration at any given forward bias, $p = p_0 \exp(\Delta E_{\text{fp}}/kT)$, where ΔE_{fp} is the change in hole quasi-Fermi level relative to equilibrium. The cathode recombination current J_{cath} is in turn given by^[27]

$$J_{\text{cath}} = q S_p p \propto \exp\left(\frac{\phi_{\text{cath}}}{kT}\right) \quad (2)$$

with q the elementary charge and S_p the surface recombination velocity for holes at the cathode. It is evident, therefore, that the contact barrier directly affects hole recombination at the cathode. When contact recombination is dominant (high ϕ_{cath}), V_{oc} will follow ϕ_{cath} linearly and when recombination at the internal donor-acceptor interface is dominant (low ϕ_{cath}), V_{oc} will be unaffected by ϕ_{cath} .^[28] Thus, it is important to minimize ϕ_{cath} by aligning WF_{cath} more closely to the PC₇₀BM electron affinity. We therefore studied WF_{cath} as a function of PFN interlayer thickness using ultraviolet photoelectron spectroscopy

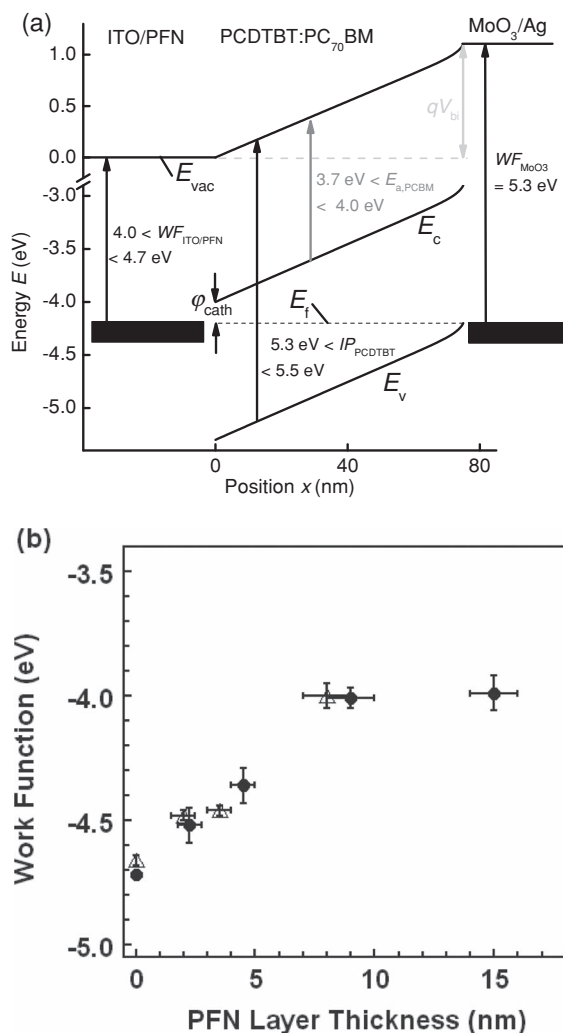


Figure 2. (a) Energy level diagram of the inverted OSC at short circuit in the dark. (b) Work function values obtained from UPS measurements (solid circles) for ITO overcoated with 0, 2, 4.5, 9 and 15 nm thick PFN films and deduced from drift-diffusion simulations (open triangles) for inverted device structures with ITO overcoated with 0, 2, 3 and 8 nm thick PFN films.

Table 1. Surface atomic percentages of detected elements for ITO coated glass overcoated with 0, 4.5, 9 and 15 nm thick PFN films.

PFN thickness (nm)	C	In	N	O	Sn	Si	others
0	41.7	18.3	0.4	34	2.2	1.6	1.8
4.5 ± 1	32.1	23.5	0.8	37.2	2.9	3.2	0.9
9 ± 1	83.7	4.0	1.9	9.0	0.5	0.7	0.1
15 ± 1	87.2	2.6	2.3	7.1	0.4	0	0.5

(UPS). As shown in Figure 2b (solid circles), the UPS measured WF_{cath} steadily changes from 4.72 to 4.00 eV as the PFN interlayer thickness increases from 0 to 9 nm and stays almost constant thereafter; thicker PFN interlayers do not further enhance WF_{cath} . The measured UPS spectra as a function of PFN thickness are shown in Figure S2 Supporting Information.

X-ray photoelectron spectroscopy (XPS) was also employed to study the PFN coated ITO as a function of PFN interlayer thickness, in this case to identify and determine the concentration of elements present at, or near, the surface. The deduced atomic percentages of the elements detected are summarized in Table 1 - minimum detectable concentrations in XPS are usually between 0.1 and 0.5 atomic% for all elements bar H and He which are undetectable. The bare ITO coated glass surface shows a substantial amount of carbon which must be present as a contaminant. With thin (4.5 nm thick) PFN interlayers, we detect significant amounts of In and Sn originating from the underlying ITO. This might suggest that the ITO is not fully covered but as the detection depth in XPS is up to ~10 nm, we can expect to see elements from the underlying substrate through the 4.5 nm PFN interlayer even for complete coverage. The detection of Si for the bare ITO coated glass and at higher concentration in the presence of 4.5 nm PFN is unexpected since the underlying silica substrate should not be visible to XPS through the ITO layer. Increasing the thickness of the PFN interlayer to 9 nm reduces the concentration of In and Sn while that of C and N (present in PFN) increases. At 15 nm PFN interlayer thickness there is still a detectable amount of In and Sn consistent with the presence of asperities that protrude from the ITO surface but no Si.

Finally, we have fabricated a series (listed in Table 2) of inverted OSC devices with increasing thickness (0 to 17 nm) PFN interlayers. For reference purposes, standard (non-inverted)

Table 2. Summary of device performance as a function of PFN film thickness for inverted OSC structures. Results are also presented for standard (non-inverted) structures. J_{sc} is the short circuit current, V_{oc} the open circuit voltage, FF the cell fill factor, PCE the power conversion efficiency, R_{sh} the shunt resistance multiplied with the device area and R_s the series resistance multiplied with the device area.

PFN thickness (nm)	J_{sc} (mA/cm ²)	V_{oc} (V)	FF (%)	PCE (%)	R_{sh} (Ω cm ²)	R_s (Ω cm ²)
0	10.25 ± 0.1	0.57	30	1.82	104.7	37.7
2	10.47 ± 0.1	0.61	37	2.33	137.1	31.9
3.5 ± 1	10.87 ± 0.1	0.67	40	3.12	192.7	21.3
8 ± 1	11.71 ± 0.1	0.91	57	5.94	473.9	2.7
12 ± 1	11.64 ± 0.1	0.91	56	5.88	442.8	5.3
17 ± 2	11.56 ± 0.1	0.90	54	5.65	454.6	12.0
Standard (non-inverted) Structure	11.81 ± 0.1	0.90	52	5.65	363.6	6.9

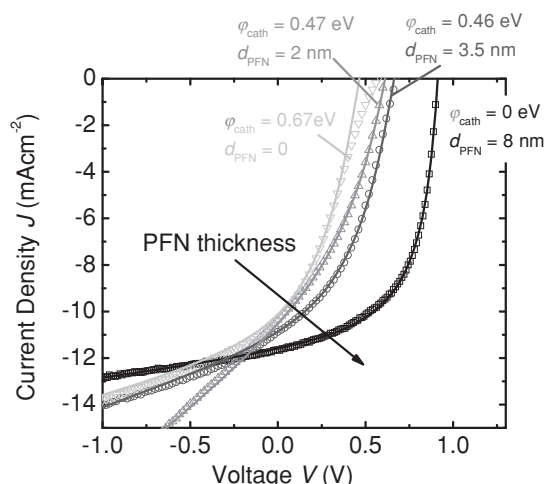


Figure 3. *J-V* curves for inverted structure OSC devices with PFN thicknesses 0 nm (open down-triangles data), 2 nm (open triangles data), 3.5 nm (open circles data), and 8 nm (open squares data). The lines are data fits to drift diffusion simulations using the parameters given in Supporting Information Table S1.

devices were also fabricated. The inverted devices comprise an ITO coated glass substrate as cathode, up to 17 nm of PFN interlayer, 80 nm PCDTBT:PC₇₀BM (1:2) charge photogeneration layer and 10 nm evaporated MoO₃ capped with 100 nm evaporated silver as anode. The standard (non-inverted) devices comprise glass/ITO/PEDOT:PSS (30 nm)/PCDTBT:PC₇₀BM (1:2) (80 nm)/Ca (30 nm)/Al (100 nm). An energy level diagram for the different component materials is shown in Figure 2a. **Figure 3** shows typical current density versus voltage (*J-V*) curves for inverted devices with PFN interlayer thicknesses between 0 and 8 nm, measured under AM 1.5G illumination at 100 mWcm⁻². The *J-V* data for up to 8 nm PFN and standard (non-inverted) devices are shown in Figure S3a Supporting Information. In addition, the external quantum efficiency (EQE) spectra for an 8 nm PFN interlayer inverted structure and for a standard (non-inverted) device are compared in Figure S3b Supporting Information; they show a very similar spectral response implying no significant change in photogeneration behaviour. The OSC parameters deduced from the *J-V* characteristics for all of the devices are listed in Table 2 and show a strong dependence on interlayer thickness as also evident from Figure 3.

Raising the PFN interlayer thickness from 0 to 8 nm substantially improves performance with increased short-circuit current density J_{sc} (from 10.25 to 11.71 mA/cm²), open-circuit voltage V_{oc} (0.57 to 0.91 V) and fill factor FF (30% to 57%). Combining these three effects results in a more than threefold improvement in overall power conversion efficiency (PCE) from 1.82% to 5.94%, thereby exceeding the 5.65% PCE measured for standard (non-inverted) devices. Further rises in interlayer thickness, e. g., to 12 nm, do not improve the performance of the devices further. Instead, J_{sc} is slightly reduced, which can at least partly be attributed to the reduced cathode/interlayer transmittance below 450 nm (c.f. Figure 1a).

Examining in more detail the PFN thickness dependent increase in V_{oc} for interlayers up to 8 nm (see Figure 3 and

Supplementary Information Figure S3a) we note that this can be rationalised in accordance with our earlier discussion of the influence of the contact barrier ϕ_{cath} on recombination current J_{cath} . Introduction of the PFN interlayer decreases WF_{cath} and hence ϕ_{cath} leading directly, via Equation (2), to a reduction in J_{cath} . To check quantitative agreement, we have theoretically estimated the change in cathode workfunction necessary to explain the observed shifts in V_{oc} . This was done using a drift-diffusion simulation of the *J-V* curves as described previously,^[29] allowing ϕ_{cath} as well as the series and parallel resistance to vary but keeping all other parameters constant (c.f. Supporting Information Table S1). From these simulations (plotted with the experimental data in Figure 3b) we deduce changes in ϕ_{cath} that transpose into WF_{cath} changes via $\phi_{cath} = WF_{cath} - E_{a,PCBM}$, with $E_{a,PCBM} = 4.0$ eV.^[17] Figure 2 compares the deduced WF_{cath} values (open triangles) with those obtained from UPS measurements (solid circles). The close agreement supports our conclusion that reduction in recombination of holes at the cathode is the dominant cause of the increasing V_{oc} with PFN thickness up to 8 nm.

The increase in J_{sc} and FF with PFN thickness is more difficult to rationalize. As can be seen from the current/voltage curves in Figure 3, the devices with PFN thicknesses below 8 nm suffer from high series and low shunt resistances. One possible explanation for the low shunt resistances is that the shunts might be caused by local single carrier conduction as described in reference [30]. It is probable that this effect is more likely to happen in devices with lower built-in voltages and therefore worse rectification properties. With a PFN thickness of 8 nm, the devices show an optimized combination of high FF , low series and high shunt resistances. A further increase of the PFN thickness leads, due to the low conductivity of the PFN film, to a slight increase of the series resistance and therefore to a reduced FF .

In conclusion, we have fabricated inverted PCDTBT:PC₇₀BM OSCs using PFN, an alcohol-soluble conjugated polyelectrolyte, as a cathode interlayer atop ITO-on-glass electrode substrates. There is a non-monotonic variation of device performance with PFN thickness, peaking at ~ 8 nm. Such thickness-optimised devices have PCE values of 5.94%, slightly higher than standard (non-inverted) devices fabricated with the same (80 nm) PCDTBT:PC₇₀BM active layer thickness but with the benefit of avoiding the requirement for reactive cathode metals. Measurements of the optical transmittance, cathode work function (via UPS) and surface atomic composition (via XPS) provide insights into this optimization. In particular, drift-diffusion simulations are consistent with the UPS measurements of decreasing cathode work function and point to a reduction in recombination of holes at the cathode as the main cause for improving V_{oc} . Beyond 8 nm PFN thickness the work function of the cathode remains essentially constant and no further improvements are seen in device performance.

Experimental Section

PCDTBT from Solenne was purified by extracting the PCDTBT with methanol, acetone and hexane, followed by dissolved in chloroform, then the filtrate was precipitated in methanol and dried under vacuum for 24 hours. 88 nm thick films for UV-Vis measurements were spin-coated

from 0.2 μm filtered, 10 mg/ml chlorobenzene (CB) solutions on top of Spectrosil B fused-silica substrates. ITO-coated glass substrates (from PsiOTec Ltd, 15 Ohms/Square), ultrasonically cleaned stepwise in acetone and isopropyl alcohol (15 min each), were oxygen plasma treated (100 W, 3 minutes) before use. For OSC device substrates the ITO was patterned to leave a central stripe; overlap between the top electrode and this stripe then defines the active device area. PFN was synthesised and purified as previously reported^[18] and 0.2 μm filtered, 1, 2, 10, and 20 mg/ml methanol solutions were spin-coated on top of Spectrosil B substrates for UV-Vis and photoluminescence measurements and on pretreated ITO substrates for contact angle, UPS and XPS measurements and for device fabrication. The PFN film thickness was controlled by varying the spin speed between 800 and 8000 rpm for each solution concentration. The PFN film thicknesses obtained for different spin speeds are shown in Figure S4. PEDOT:PSS (Clevios™ Al 4083) was used as purchased from Heraeus. Scientific grade (99.5%) [6,6]-phenyl-C₇₁-butyric acid methyl ester (PC₇₀BM) was used as received from Solenne. Blend solutions of PCDTBT and PC₇₀BM were mixed at a weight ratio of 1:2 in CB (24 mg/ml), stirred at 70 °C overnight to promote complete dissolution, and spin-coated to yield 80 nm thick OSC active layers in each of the device structures studied (standard and inverted with different PFN interlayer thicknesses).

Transmittance spectra were recorded using an ultraviolet-visible spectrophotometer (Jasco V-560). The thickness of films was measured using a surface profilometer (Tencor Instruments Alpha Step 200). Sheet resistance was determined using a home-built four-point probe apparatus. Contact angle measurements were performed with a drop shape analysis system (Krüss DSA 100). Ultraviolet and X-ray photoelectron spectroscopy measurements were undertaken with an Axis Ultra DLD system (Kratos Analytical). For UPS measurements a He I lamp (−21.22 eV energy) was used as the excitation source. The detection area was a spot of ~110 μm diameter. A bias of −18.49 V was applied to the sample. From the onset of the secondary electron energy cutoff, E_{co} , we can calculate the work function, $WF = h\nu - (E_{\text{co}} - E_{\text{F}})$ where $h\nu$ is the excitation photon energy and E_{F} the Fermi level. For XPS measurements, an Al K α (1486.6 eV) X-ray excitation source operated at 15 kV and 5 mA was used. Spectra were collected at 0° to the surface normal over a binding energy range 1400 to −10 eV with a pass bandwidth of 160 eV using 1 eV steps, 0.2 s dwell time per step and averaging 2 scans. The detection area was ~700 $\mu\text{m} \times 300 \mu\text{m}$. CasaXPS software was used to determine peak areas, with the NPL intensity (transmission function) calibration and average relative sensitivity factors; the detectable element concentrations were thereby enumerated.

The inverted OSC structures comprise glass/ITO/PFN/PCDTBT:PC₇₀BM/MoO₃/Ag. The standard (non-inverted) reference structures comprise glass/ITO/PEDOT:PSS/PCDTBT:PC₇₀BM/Ca/Al. The inverted structures were fabricated by spin-coating PFN (0–12 nm thickness) followed by PCDTBT:PC₇₀BM (1:2 by weight, 80 nm thickness) onto pretreated ITO substrates. For standard structures, a thin layer (30 nm) of PEDOT:PSS was spin-coated onto the pretreated ITO and baked at 120 °C for 20 minutes in air. PCDTBT:PC₇₀BM (1:2 by weight, 80 nm thickness) was then spin-coated on top. In both cases, the spin-coated structures were then transferred into a nitrogen-filled glove box (<0.1 ppm O₂ and H₂O) and baked at 60 °C for 30 minutes. Finally, top electrodes were thermally evaporated through a shadow mask onto the PCDTBT:PC₇₀BM. The 10 nm MoO₃, 100 nm Ag, 30 nm Ca and 100 nm Al layers were all thermally deposited *in vacuo* at room temperature at a base pressure of 5×10^{-6} Torr. The top 1.5 mm wide Ca/Al cathode or MoO₃/Ag anode contacts were aligned orthogonal to the ITO stripe on the substrate, with an overlap of $3 \times 1.5 \text{ mm}^2 = 4.5 \text{ mm}^2$ that defines the active device area. Six individual devices were prepared simultaneously on each substrate.

OSC performance was tested with the devices held in a nitrogen-filled chamber. The current-density-voltage (J-V) characteristics were measured using a Keithley 2400 source measure unit. The photocurrent was measured under AM 1.5G illumination (through the glass substrate) at 100 mWcm^{−2} using a Newport Thermo Oriel 91192 1000W Solar Simulator. External quantum efficiency (EQE) spectra were recorded

using the monochromated (Bentham) output from a tungsten halogen lamp calibrated with a Newport UV-181 photodiode; phase sensitive detection with a lock-in amplifier was used to increase signal to noise.

Supporting Information

Supporting Information is available from the Wiley Online Library or from the author.

Acknowledgements

We thank the UK Engineering and Physical Sciences Research Council for funding (grant EP/F061757/1) and the Centre for Plastic Electronics for providing research facilities. DDCB is the Lee-Lucas Professor of Experimental Physics. TK acknowledges support via an Imperial College Junior Research Fellowship.

Received: November 22, 2012

Revised: December 21, 2012

Published online: March 7, 2013

- [1] H. Hoppe, N. S. Sariciftci, *J. Mater. Res.* **2004**, *19*, 1924.
- [2] M. C. Scharber, D. Mühlbacher, M. Koppe, P. Denk, C. Waldauf, A. J. Heeger, C. J. Brabec, *Adv. Mater.* **2006**, *18*, 789.
- [3] Y. Kim, S. Cook, S. M. Tuladhar, S. A. Choulis, J. Nelson, J. R. Durrant, D. D. C. Bradley, M. Giles, I. McCulloch, C. M. Ree, *Nature Materials* **2006**, *5*, 197.
- [4] C. G. Shuttle, B. O'Regan, A. M. Ballantyne, J. Nelson, D. D. C. Bradley, J. C. de Mello, J. R. Durrant, *Appl. Phys. Lett.* **2008**, *92*, 093311.
- [5] C. J. Brabec, S. Gowrisanker, J. J. M. Halls, D. Laird, S. J. Jia, S. P. Williams, *Adv. Mater.* **2010**, *22*, 3839.
- [6] R. Xia, M. Al-Hashimi, W. C. Tsoi, M. Heeney, D. D. C. Bradley, J. Nelson, *Solar Energy Mater. Solar Cells* **2012**, *96*, 112.
- [7] J. Y. Kim, S. H. Kim, H. H. Lee, K. Lee, W. Ma, X. Gong, A. J. Heeger, *Adv. Mater.* **2006**, *18*, 572.
- [8] R. Pacios, A. J. Chatten, K. Kawano, J. R. Durrant, D. D. C. Bradley, J. Nelson, *Adv. Funct. Mater.* **2006**, *16*, 2117.
- [9] C. Yang, J. Y. Kim, S. Cho, J. K. Lee, A. J. Heeger, F. Wudl, *J. Am. Chem. Soc.* **2008**, *130*, 6444.
- [10] D. S. Leem, A. Edwards, M. Faist, J. Nelson, D. D. C. Bradley, J. C. de Mello, *Adv. Mater.* **2011**, *23*, 437.
- [11] G. K. Mor, K. Shankar, M. Paulose, O. K. Varghese, C. A. Grimes, *Appl. Phys. Lett.* **2007**, *91*, 152111.
- [12] S. K. Hau, H. L. Yip, O. Acton, N. S. Baek, H. Ma, A. K. Y. Jen, *J. Mater. Chem.* **2008**, *18*, 5113; M. M. Voigt, R. C. I. Mackenzie, S. P. King, C. P. Yau, P. Atienzar, J. Dane, P. E. Keivanidis, I. Zadrzil, D. D. C. Bradley, J. Nelson, *Solar Energy Mater. Solar Cells* **2012**, *105*, 77.
- [13] H. H. Liao, L. M. Chen, Z. Xu, G. Li, Y. Yang, *Appl. Phys. Lett.* **2008**, *92*, 173303.
- [14] B. Y. Yu, A. Tsai, S. P. Tsai, K. T. Wong, Y. Yang, C. W. Chu, J. J. Shyue, *Nanotechnology* **2008**, *19*, 255202.
- [15] H. Ma, H.-L. Yip, F. Huang, A. K.-Y. Jen, *Adv. Funct. Mater.* **2010**, *20*, 1371–1388.
- [16] X. Wang, T. Ishwara, W. Gong, M. Campoy-Quiles, J. Nelson, D. D. C. Bradley, *Adv. Funct. Mater.* **2012**, *22*, 1454.
- [17] L. Dou, J. You, J. Yang, C. Chen, Y. He, S. Murase, T. Moriarty, K. Emery, G. Li, Y. Yang, *Nat. Photon.* **2012**, *6*, 180.

- [18] Z. He, C. Zhong, X. Huang, W. Y. Wong, H. Wu, L. Chen, S. Su, Y. Cao, *Adv. Mater.* **2011**, 23, 4636.
- [19] Y. Zhou, C. Fuentes-Hernandez, J. Shim, J. Meyer, A. J. Giordano, H. Li, P. Winget, T. Papadopoulos, H. Cheun, J. Kim, M. Fenoll, A. Dindar, W. Haske, E. Najafabadi, T. M. Khan, H. Sojoudi, S. Barlow, S. Graham, J. L. Bredas, S. R. Marder, A. Kahn, B. Kippelen, *Science* **2012**, 336, 327.
- [20] Z. He, C. Zhong, S. Su, M. Xu, H. Wu, Y. Cao, *Nat. Photon.* **2012**, 6, 591.
- [21] J. H. Seo, A. Gutacker, Y. Sun, H. Wu, F. Huang, Y. Cao, U. Scherf, A. J. Heeger, G. C. Bazan, *J. Am. Chem. Soc.* **2011**, 133, 8416.
- [22] J. H. Seo, A. Gutacker, B. Walker, S. Cho, A. Garcia, R. Yang, T. Q. Nguyen, A. J. Heeger, G. C. Bazan, *J. Am. Chem. Soc.* **2009**, 131, 18220.
- [23] N. Blouin, A. Michaud, M. Leclerc, *Adv. Mater.* **2007**, 19, 2295.
- [24] S. H. Park, A. Roy, S. Beaupre, S. Cho, N. Coates, J. S. Moon, D. Moses, M. Leclerc, K. Lee, A. J. Heeger, *Nat. Photon.* **2009**, 3, 297.
- [25] S. Cho, J. H. Seo, S. H. Park, S. Beaupré, M. Leclerc, A. J. Heeger, *Adv. Mater.* **2010**, 22, 1253.
- [26] J. H. Seo, S. Cho, M. Leclerc, A. J. Heeger, *Chem. Phys. Lett.* **2011**, 503, 101.
- [27] S. Schafer, A. Petersen, T. A. Wagner, R. Kniprath, D. Lingenfelter, A. Zen, T. Kirchartz, B. Zimmermann, U. Wurfel, X. Feng, T. Mayer, *Phys. Rev. B* **2011**, 83, 165311; T. Kirchartz, W. Gong, S. A. Hawks, T. Agostinelli, R. C. I. MacKenzie, Y. Yang, J. Nelson, *J. Phys. Chem. C* **2012**, 116, 7672.
- [28] J. C. Blakesley, D. Neher, *Phys. Rev. B* **2011**, 84, 075210.
- [29] T. Kirchartz, B. E. Pieters, J. Kirkpatrick, U. Rau, J. Nelson, *Phys. Rev. B* **2011**, 83, 115209.
- [30] S. Dongaonkar, J. D. Servaites, G. M. Ford, S. Loser, J. Moore, R. M. Gelfand, H. Mohseni, H. W. Hillhouse, R. Agrawal, M. A. Ratner, T. J. Marks, M. S. Lundstrom, M. A. Alam, *J. Appl. Phys.* **2010**, 108, 124509.